

A Candidate of a Least-Massive Black Hole at the First 1.1 Billion Years of the UniverseMASAFUSA ONOUE,^{1,2,*} KOHEI INAYOSHI,¹ XUHENG DING,² WENXIU LI,¹ ZHENGRONG LI,¹ JUAN MOLINA,¹
AKIO K. INOUE,^{3,4} LINHUA JIANG,^{1,5} AND LUIS C. HO^{1,5}¹*Kavli Institute for Astronomy and Astrophysics, Peking University, Beijing 100871, China*²*Kavli Institute for the Physics and Mathematics of the Universe (Kavli IPMU, WPI), The University of Tokyo, Chiba 277-8583, Japan*³*Waseda Research Institute for Science and Engineering, Faculty of Science and Engineering, Waseda University, 3-4-1, Okubo, Shinjuku, Tokyo 169-8555, Japan*⁴*Department of Physics, School of Advanced Science and Engineering, Faculty of Science and Engineering, Waseda University, 3-4-1, Okubo, Shinjuku, Tokyo 169-8555, Japan*⁵*Department of Astronomy, School of Physics, Peking University, Beijing 100871, China***ABSTRACT**

We report a promising candidate of a low-luminosity active galactic nucleus (AGN) at $z = 5$ that was selected from the first near-infrared images of the JWST CEERS project. This source, named CEERS-AGN-z5-1 at absolute 1450 Å magnitude $M_{1450} = -19.5 \pm 0.3$, was found via a visual selection of compact sources from a catalog of Lyman break galaxies at $z > 4$, taking advantage of the superb spatial resolution of the JWST/NIRCam images. The 21 photometric data available from CFHT, HST, Spitzer, and JWST suggest that the continuum shape of this source is reminiscent of that for an unobscured AGN, and there is a clear color excess in the filters where the redshifted $H\beta + [\text{O III}]$ and $H\alpha$ are covered. The estimated line luminosity is $L_{H\beta + [\text{O III}]} = 10^{43.0} \text{ erg s}^{-1}$ and $L_{H\alpha} = 10^{42.9} \text{ erg s}^{-1}$ with the corresponding rest-frame equivalent width $\text{EW}_{H\beta + [\text{O III}]} = 1100 \text{ Å}$ and $\text{EW}_{H\alpha} = 1600 \text{ Å}$, respectively. Our SED fitting analysis favors the scenario that this object is either a strong broad-line emitter or even a super-Eddington accreting black hole (BH) emerging in a metal-poor host galaxy. The bolometric luminosity, $L_{\text{bol}} = 2.5 \pm 0.3 \times 10^{44} \text{ erg s}^{-1}$, is consistent with those of $z < 0.35$ broad-line AGNs with $M_{\text{BH}} \sim 10^6 M_{\odot}$ accreting at the Eddington limit. This new AGN population at the first 1.1 billion years of the universe may close the gap between the observed BH mass range at high redshift and that of BH seeds. Spectroscopic confirmation is awaited to secure the redshift and its AGN nature.

1. INTRODUCTION

The past two decades were a golden era of high-redshift quasar observations. Starting from the Sloan Digital Sky Survey (Fan et al. 2001a; Jiang et al. 2016), $\gtrsim 1000 \text{ deg}^2$ -class wide-field surveys have identified several hundred quasars in the epoch of cosmic reionization with the current redshift record of $z \sim 7.6$ (Bañados et al. 2018; Yang et al. 2021; Wang et al. 2021). Follow-up spectroscopic studies have revealed that those quasars are powered by accreting massive BHs with masses greater than $M_{\text{BH}} = 10^9 M_{\odot}$, despite their young ages (e.g., Wu et al. 2015; Shen et al. 2019). The formation and early growth history of massive BHs is one of the biggest mysteries of modern astronomy.

Exploring the origin of the massive BHs is still challenging because the brightest quasar population is already matured after experiencing rapid accretion episodes and losing the information on their seeding process. Currently, the least massive BHs that have been spectroscopically confirmed at $z \gtrsim 5$ are those with $M_{\text{BH}} \sim 10^8 M_{\odot}$ (e.g., Willott et al. 2010; Onoue et al. 2019), several orders of magnitudes heavier than the predicted seed mass range ($10^{2-6} M_{\odot}$; see Inayoshi et al. 2020, for a recent review). Therefore, it is crucial to close the gap between the two mass regimes via detecting lower-mass BHs in epochs as early as possible.

Extensive efforts have been made with the Hubble Space Telescope (HST) to identify $z \gtrsim 6$ AGNs at the very faint end of the quasar/AGN luminosity function (UV magnitude -22 or fainter); however, no promising objects have been reported yet (Morishita et al. 2020; Jiang et al. 2022). A naive interpretation of their low success rates is that their point-source selection is not

Corresponding author: Masafusa Onoue
onoue@pku.edu.cn

* Kavli Astrophysics Fellow

an effective approach to search for low-luminosity AGNs, because host galaxy contamination becomes more severe (Bowler et al. 2021; Adams et al. 2022a). On the other hand, a fraction of high-redshift quasars seem to have compact (< 1 kpc) host galaxies, according to recent ALMA observations of luminous $z > 6$ quasars (Neeleman et al. 2021; Walter et al. 2022).

Aside from pure AGN surveys, one possible alternative approach to find low-luminosity AGNs is to use samples of UV-selected galaxies. At redshift $4 < z < 6$, the UV luminosity functions of AGNs and Lyman break galaxies (LBGs) intersect with each other at $M_{UV} \sim -23$ mag (Harikane et al. 2022a; Mat-suoka et al. 2018). Spectroscopic follow-up studies of $z \gtrsim 4$ LBGs have recently found several candidates of AGNs and galaxy+AGN composite sources at the galaxy-dominated regime, based on detection of broad emission lines and high-ionization emission lines such as He II and N V (Laporte et al. 2017; Harikane et al. 2022a).

The James Webb Space Telescope (JWST) has just provided its first infrared images in July 2022. The 6.5-meter space observatory is expected to be a game changer in the field of extragalactic observations. Numerous papers have claimed the first detection of ultra high-redshift galaxies at $z \gtrsim 10$, waiting for spectroscopic confirmation (e.g., Castellano et al. 2022; Donnan et al. 2022; Adams et al. 2022b; Finkelstein et al. 2022; Harikane et al. 2022b; Naidu et al. 2022). Likewise, the superb sensitivity of JWST may also enable us to witness rapidly accreting seed BHs far beyond the current samples of high-redshift AGNs. (e.g., Natarajan et al. 2017; Valiante et al. 2018; Inayoshi et al. 2022b; Goulding & Greene 2022).

We here report a candidate low-luminosity AGN at $z = 5$, slightly after the end of cosmic reionization. This candidate was selected with the first imaging dataset of the Cosmic Evolution Early Release Science Survey (CEERS; Finkelstein et al. 2017), one of the JWST Cycle 1 Early Release Science programs. In Section 2, we present our imaging dataset and parent sample of $z > 4$ LBGs. Section 3 presents our discovery of a promising AGN candidate and its photometric properties. Our spectral fitting analysis and constraint on the $z = 5$ AGN luminosity function is discussed in Section 4, followed by our future prospects in Section 5. All magnitudes quoted in this paper are in the AB system. Λ CDM cosmology is adopted with $H_0 = 70$ km s $^{-1}$ Mpc $^{-1}$, $\Omega_M = 0.3$, and $\Omega_\Lambda = 0.7$, leading to a scale of 6.28 kpc per arcsec at $z = 5$.

2. CANDIDATE SELECTION

2.1. Sample

The parent sample of our selection is a catalog of $z = 2$ –9 LBGs compiled by Bouwens et al. (2021). This sample was obtained from multiple imaging surveys of the HST. The CANDELS Extended Groth Strip (EGS) field is covered by the JWST CEERS program. A multi-wavelength (0.4–8 μ m) source catalog down to HST/WFC3 F160W magnitude 26.62 was made available by Stefanon et al. (2017).

This LBG catalog with multi-wavelength photometry is ideal to characterize the near-infrared (NIR) spectral energy distribution (SED) of $z > 4$ LBGs and search for low-luminosity AGNs. We thus initiated our low-luminosity AGN survey by finding JWST counterparts of those known LBGs.

2.2. Data Reduction

The data we analyze in this paper are the first CEERS images taken by the *Near Infrared Camera* (NIRCam; Rieke et al. 2005) on 21 June 2022. The CEERS survey employs seven filters of NIRCam (F115W, F150W, F200W, F277W, F356W, F410M, and F444W) that cover 1–5 μ m. At the time of writing this paper, the full-band coverage of NIRCam is four pointings (CEERS1, CEERS2, CEERS3, CEERS6) of the NIRCam’s $2'.2 \times 4'.4$ field-of-views, or 34.5 arcmin 2 . The total exposure times for each filter is about 2835 seconds, while F115W has twice longer exposure times (Finkelstein et al. 2022). More details of the survey design will be presented by the survey team (Finkelstein et al. in prep.).

We downloaded the archival Stage 2 data products from the STScI MAST Portal¹. The Stage 2 images were processed with the JWST pipeline version 1.5.3 with the pipeline mapping file `jwtst_0942.pmap` except for F410M and F444W. For those two reddest filters multiple pmap files are used (`jwtst_0877.pmap` and `jwtst_0878.pmap` for F410M; `jwtst_0877.pmap`, `jwtst_0878.pmap`, and `jwtst_0881.pmap` for F444W), depending on the fields. The Stage 2 images were post-processed as follows. It is known that the version 1.5.3 pipeline has an issue in the imaging background subtraction². We first subtracted the global background with `photutils`’s `Background2D` function. There is a clear horizontal and vertical pattern in the current NIRCam images due to detector read-noise. The so-called $1/f$ noise was removed with the script provided by the CEERS team³.

¹ <https://archive.stsci.edu/>

² <https://github.com/spacetelescope/jwst/issues/6920>

³ <https://ceers.github.io/releases.html#sdr1>

Those post-processed Stage 2 frames were then stacked by the JWST Stage 3 pipeline. During the Resample step, we decreased the final pixel sampling size by a factor of two with the drizzle algorithm. This procedure yields the final pixel sizes of 0.0156 arcsecond per pixel in Short Wavelength filters (F115W, F150W, and F200W) and 0.0315 arcsecond per pixel in Long Wavelength filters (F277W, F356W, F410M, and F444W). The Stage 3 images were aligned to match the coordinates of unsaturated GAIA sources inside each field-of-view based on its DR3 source catalog (Gaia Collaboration et al. 2016). Finally, we referred to the post-flight flux calibration files that contain conversion factors from pixel signals per second to mega Jansky per steradian unit (jwst_nircam_photom_0101.fits for module A, and jwst_nircam_photom_0104.fits for module B). This process was needed to correct the pre-flight measurements applied in the original images. The difference of the pre- and post-flight photometric reference files is significant, as is also discussed in Adams et al. (2022b). With the updated calibration, the F410M and F444W flux densities (in mega Jansky per steradian unit) decrease by 10–20 percent in the two NIRCcam detector modules.

We also examined the consistency of photometry between images of JWST/NIRCcam and HST/WFC3 that cover similar wavelength ranges. We performed aperture photometry for bright stars inside the current footprints of CEERS. For HST, we use the WFC3 images processed by the CEERS team⁴. With aperture correction taken into account, we found that the NIRCcam F115W magnitudes offset from the HST/WFC3 F125W magnitudes by -0.05 mag. Likewise, the NIRCcam F150W magnitudes have ~ -0.20 – -0.15 mag offsets with respect to WFC3 F140W and F160W magnitudes. Since the two WFC3 filters straddle the transmission curve of NIRCcam F150W, this offset cannot be explained by stellar SEDs. Therefore, we added $+0.05$ mag to our photometry for F115W and $+0.15$ mag for F150W. The amount of possible offsets for the other filters (F200W, F277W, F356W, F410M, F444M) is uncertain at this stage, because there are no HST filters that match with those NIRCcam filters. The absolute flux calibration that we use has 20% uncertainty in all filters, which is consistent with our offset measurements for F115W and F150W. We thus added 0.2 magnitude to the uncertainty of photometry for all NIRCcam filters, which dominates the error budget for our LBGs. Further analyses of the on-

going JWST calibration programs are needed to better perform photometry with NIRCcam.

2.3. Visual Selection of Point Sources

The NIRCcam images of $z > 4$ LBGs in the CEERS field were visually inspected by one of the authors (M. Onoue). We focused on compact sources, because we are interested in sources dominated by the central BH radiation. We note that the UV luminosity function at the faint end (rest-frame UV magnitude $m_{UV} \gtrsim 24$ mag, or $M_{UV} \gtrsim -22$ mag in the absolute frame) is dominated by star-forming galaxies (Harikane et al. 2022a; Bowler et al. 2021; Adams et al. 2022a). In this sense, our morphology selection is only sensitive to a subsample of AGN populations at high redshift, the host galaxies of which are outshined by the central AGNs or have compact morphology.

The visual inspection of the known $z > 4$ LBGs returned approximately 20 compact sources without any noticeable extended components or interacting sources. We initially ran SExtractor (Bertin & Arnouts 1996) for those compact sources to measure their total magnitudes. Those sources were then cross-matched to the CANDELS multi-band catalog (Stefanon et al. 2017) to compile their optical-to-NIR photometric information.

We hereafter present one of the compact sources we found from the selection above, CEERS-AGN-z5-1, or EGSV-9176349491 in the original CANDELS catalog with the photometric redshift $z = 4.71$. This source shows a unique photometric color reminiscent of an unobscured AGN, as we present later in this paper. The NIRCcam coordinate of CEERS-AGN-z5-1 is (R.A., Decl.) = (14:19:17.629, +52:49:49.04). The WFC3 F160W magnitude of CEERS-AGN-z5-1 is 26.71 ± 0.17 .

3. RESULTS

3.1. A Candidate AGN at $z = 5$

CEERS-AGN-z5-1 shows a remarkably red NIRCcam color among the selected compact LBGs, based on our initial SExtractor photometry. This was later confirmed by our additional photometry with a two-dimensional image modeling tool Galight (Ding et al. 2020, 2021), which we report in Table 1. The photometry with Galight assumes that the central source is a combination of point spread function (PSF) and a two-dimensional Sérsic profile. The PSF models applied in each filter are based on a library of point source profiles sampled from the CEERS images. More details on the Galight analysis with JWST images are presented in Ding et al. (2022). In this paper, we use the total magnitudes to characterize the SED of CEERS-AGN-z5-1 in the follow-

⁴ CEERS HST data release v1: <https://ceers.github.io/releases.html#hdr1>

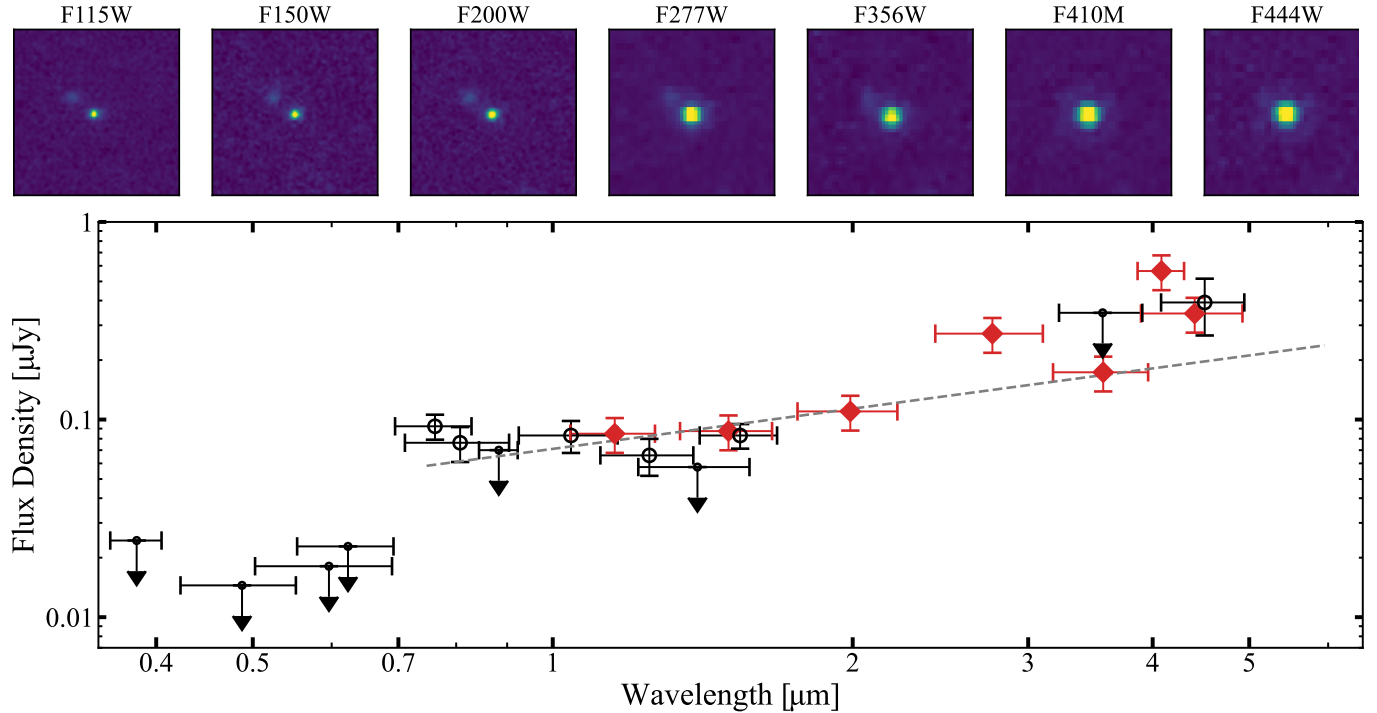


Figure 1. The $z = 5$ AGN candidate presented in this paper, CEERS-AGN-z5-1. (*Top:*) The snapshot images of seven NIRCcam filters employed in CEERS. The image size of each panel is $1''.5 \times 1''.5$. There is a companion source to the upper left from the central source. (*Bottom:*) The optical-to-NIR SED of CEERS-AGN-z5-1. The NIRCcam flux densities based on model magnitudes are presented in red. CEERS-AGN-z5-1 has an entry in the CANDELS catalog of [Stefanon et al. \(2017\)](#). Here we show optical CFHT/MegaCam (u^* , g' , r' , i' , z'), HST/ACS (F606W, F888W) + WCS3 (F105W, F125W, F140W, F160W), and Spitzer/IRAC (3.6 μm and 4.5 μm) in black. Three sigma upper-limit flux densities are shown for those with signal-to-noise ratios less than 3. Horizontal and vertical error bars correspond to the filter bandwidths and photometric errors, respectively. The grey dashed line shows our best-fit power-law continuum model, where the continuum slope index is $\alpha_\lambda = -1.32 \pm 0.30$.

ing analysis. The CFHT, HST, and Spitzer magnitudes available for this source are also reported in Table 1, while for HST/WFC3 F105W, F125W and F160W, we also applied Galight to update the photometry from the catalog.

We note that there is a faint companion source to the upper left of the NIRCcam images (Figure 1). The NIRCcam coordinate of this source is (R.A., Decl.) = (14:19:17.628, +52:49:48.79), approximately 0.23 arcsecond to the south of CEERS-AGN-z5-1. The 2D flux distribution of this companion is simultaneously fitted with Galight to deblend the two sources, as we report in Table 1. This companion is not identified in the reddest F410M and F444W filters. The effect of blending on the photometry of those two filters is likely minor, because the companion is ≈ 1 mag fainter than CEERS-AGN-z5-1 in the SW filters and the difference becomes > 2 mag for F277W and F356W.

Figure 1 shows the NIRCcam cutout images and the optical-to-NIR SED of CEERS-AGN-z5-1. Thanks to the wealth of photometry available in the CEERS field, the rest-frame UV-to-optical SED of CEERS-AGN-z5-1 is clear. There is a strong Lyman break between CFHT

r' - and i' -band (and HST/ACS F814W). The observed continuum redward of Lyman break is red with F115W – F356W = $+0.8 \pm 0.3$. Moreover, there is a clear color excess at 3 μm (F277W) and 4 μm (F410M, F444W, and IRAC 4.5 μm), while F356W traces the continuum in between. This excess matches with the redshifted $\text{H}\beta + [\text{O III}]$ and $\text{H}\alpha$ emission lines, respectively. The strong excess of F410M suggests that $\text{H}\alpha$ emission line is within the F410M coverage. Those photometric features suggest that CEERS-AGN-z5-1 is a $4.9 \leq z \leq 5.6$ source with emission lines so strong that they affect broad/medium-band photometry, as we discuss in more details later (Sections 3.3 and 4.1).

3.2. Continuum Properties

The broad-band photometry of CEERS-AGN-z5-1 is well reproduced by a continuum model with a single power-law function except for filters that cover strong emission, especially $\text{H}\beta + [\text{O III}]$ and $\text{H}\alpha$. Our best-fit model based on photometry for F115W, F150W, and F200W filters suggests a power-law slope α_λ ($\equiv d \ln F_\lambda / d \ln \lambda$) of -1.32 ± 0.30 , which is consistent with a typical value for type 1 quasars (e.g., [Fan et al.](#)

Table 1. Optical-to-NIR photometry of CEERS-AGN-z5-1 and the companion source

Filter	CEERS-AGN-z5-1	Companion
JWST/NIRCam F115W	26.6 ± 0.2	27.6 ± 0.2
JWST/NIRCam F150W	26.6 ± 0.2	27.4 ± 0.2
JWST/NIRCam F200W	26.3 ± 0.2	27.5 ± 0.2
JWST/NIRCam F277W	26.3 ± 0.2	28.9 ± 0.2
JWST/NIRCam F356W	25.8 ± 0.2	28.7 ± 0.2
JWST/NIRCam F410M	24.5 ± 0.2	...
JWST/NIRCam F444W	25.1 ± 0.2	...
CFHT/MegaCam u^*	> 27.9	
CFHT/MegaCam g'	> 28.5	
CFHT/MegaCam r'	> 28.0	
CFHT/MegaCam i'	26.5 ± 0.2	
CFHT/MegaCam z'	> 26.8	
HST/ACS F606W	> 28.3	
HST/ACS F814W	26.7 ± 0.2	
HST/WFC3 F105W	26.6 ± 0.2	
HST/WFC3 F125W	26.9 ± 0.2	
HST/WFC3 F140W	> 27.0	
HST/WFC3 F160W	26.6 ± 0.2	
Spitzer/IRAC $3.6\mu\text{m}$	> 25.1	
Spitzer/IRAC $4.5\mu\text{m}$	24.9 ± 0.3	

NOTE— The photometric errors for NIRCam filters are from the 20% uncertainty of the absolute flux calibration. The CFHT, HST/ACS, and Spitzer photometry is from the multi-wavelength catalog of [Stefanon et al. \(2017\)](#). The HST/WFC3 magnitudes (F105W, F125W, F160W) are updated based on our Galight photometry. Three sigma upper limits are provided for filters with no detection, including F140W, for which we use the value in the [Stefanon et al. \(2017\)](#)’s catalog.

2001b; [Vanden Berk et al. 2001](#), hereafter VB01). With five more filters from CFHT z' -band and HST/WFC3 (F105W, F125W, F140W, and F160W), the slope gets slightly flatter with a larger error ($\alpha_\lambda = -1.27 \pm 0.92$). Note that the non-detection in HST/F140W (> 27.0) is inconsistent with the former continuum model by +0.5 mag at the effective wavelength of F140W. In what follows, we adopt the former model with NIRCam only, which is presented in the bottom panel of Figure 1 (dashed line). Note that the different choice of the spectral index causes only $< 5\%$ of the difference in the estimated continuum flux density at rest-frame 3000 and 5100 Å.

Adopting the fitted spectral index, we estimate the absolute magnitude at rest-frame 1450 Å as $M_{1450} = -19.5 \pm 0.3$ mag at $z = 5$. The monochromatic lumi-

nosity at rest-frame 3000 Å and 5100 Å are $\lambda L_{3000} = 4.6 \pm 0.5 \times 10^{43}$ erg s $^{-1}$ and $\lambda L_{5100} = 3.9 \pm 0.4 \times 10^{43}$ erg s $^{-1}$, respectively. The rest-frame UV brightness of CEERS-AGN-z5-1 is more than three magnitudes fainter than those for spectroscopically-confirmed $z \sim 5$ quasars from the moderately deep optical survey by Subaru/HSC ([Niida et al. 2020](#)). We estimate the bolometric luminosity by applying the bolometric correction for λL_{3000} ([Richards et al. 2006](#))⁵, which yields $L_{\text{bol}} = 5.15 \times \lambda L_{3000} = 2.5 \pm 0.3 \times 10^{44}$ erg s $^{-1}$. The expected BH mass is $M_{\text{BH}} = 2 \times 10^6 M_\odot$ if we assume Eddington-limit accretion. The inferred bolometric luminosity becomes $L_{\text{bol}} = 4.1 \pm 0.4 \times 10^{44}$ erg s $^{-1}$, when we use the correction factor of 9.26 for λL_{5100} instead.

Figure 2 shows the BH mass - bolometric luminosity plane for AGNs at different redshift ranges. The inferred bolometric luminosity of CEERS-AGN-z5-1 is more than two dex smaller than those of the typical $z = 1$ –2 SDSS DR7 quasars with $L_{\text{bol}} \simeq 10^{46.5}$ erg s $^{-1}$ ([Shen et al. 2011](#)) and those of known $z \gtrsim 5$ quasars with virial BH masses available from Mg II ([Willott et al. 2010](#); [Trakhtenbrot et al. 2011](#); [Onoue et al. 2019](#); [Matsuoka et al. 2019](#); [Kato et al. 2020](#)). The luminosity of CEERS-AGN-z5-1 is rather comparable to those for typical low-redshift ($z < 0.35$) broad-line AGNs ([Liu et al. 2019](#)). In Figure 2, we show that some $M_{\text{BH}} \sim 10^6 M_\odot$ BHs from [Greene & Ho \(2007\)](#) and [Liu et al. \(2018\)](#) have comparable luminosities to CEERS-AGN-z5-1. An even less massive BH can power this source if rapid super-Eddington accretion is achieved. The necessity of such intermittent super-Eddington phases has been recently argued in theoretical predictions of early BH assembly ([Inayoshi et al. 2022a](#); [Hu et al. 2022](#); [Shi et al. 2022](#)). On the other hand, the same luminosity can also be achieved by a sub-Eddington BH with $M_{\text{BH}} \simeq 10^{7-8} M_\odot$, as long as the nuclear accretion disk settles down to a radiatively efficient state ($L_{\text{bol}}/L_{\text{Edd}} \gtrsim 0.01$; see [Yuan & Narayan 2014](#)). Spectroscopic follow-up observations of broad Balmer lines or other virial BH mass tracers such as Mg II $\lambda 2798$ are necessary to robustly estimate the BH mass of CEERS-AGN-z5-1.

3.3. Broad/Medium-Band Excess

We now quantify the broad/medium-band excess due to H β + [O III] and H α . Here we consider the NIRCam photometry of F277W, F410M, and F444W, and

⁵ The bolometric luminosities of the [Richards et al. \(2006\)](#)’s sample are $L_{\text{bol}} > 10^{45}$ erg s $^{-1}$, approximately a half dex higher than that of CEERS-AGN-z5-1. The luminosity dependence of bolometric correction is discussed in, for example, [Netzer \(2019\)](#). With their prescription, the bolometric correction factors become twice larger for CEERS-AGN-z5-1.

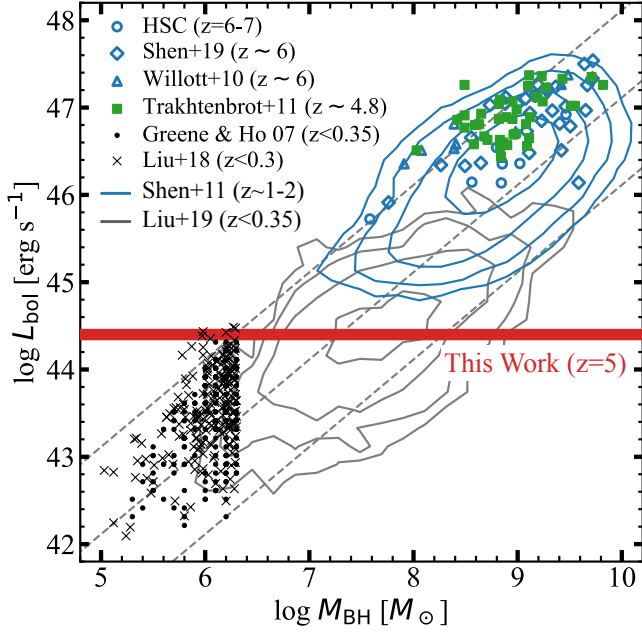


Figure 2. The BH mass - bolometric luminosity plane. The bolometric luminosity of CEERS-AGN-z5-1 ($L_{\text{bol}} = 2.5 \times 10^{44} \text{ erg s}^{-1}$; red line) is estimated from its 3000 Å monochromatic luminosity. The virial BH masses of broad-line AGNs at various redshift ranges are also shown for comparison. Blue symbols are $z > 6$ quasars from Subaru/HSC (circle; Onoue et al. 2019; Matsuoka et al. 2019; Kato et al. 2020), SDSS (diamond; Shen et al. 2019), and CFHQS (triangle; Willott et al. 2010). Green squares show $z \sim 4.8$ quasars from Trakhtenbrot et al. (2011). The blue contour is the normalized distribution of SDSS DR7 quasars with a logarithm step of 0.5 dex. (Shen et al. 2011). The BH masses from the literature above are estimated based on Mg II $\lambda 2798$. The grey contour shows the normalized distribution of low-redshift ($z \lesssim 0.35$) broad-line AGNs (Liu et al. 2019) with the same step as for the Shen et al.’s $z \sim 1-2$ distribution. Black symbols are the individual low-redshift AGNs with estimated BH masses $M_{\text{BH}} \lesssim 10^{6.3} M_{\odot}$ from Greene & Ho (2007, dot), and Liu et al. (2018, cross). Those low-redshift samples use Balmer lines to estimate BH masses. Clearly, CEERS-AGN-z5-1 has the typical luminosity of the $z < 0.35$ AGNs with $M_{\text{BH}} \gtrsim 10^6 M_{\odot}$. The three diagonal lines indicate 100%, 10%, and 1% Eddington luminosity from top left to bottom right.

use our continuum model with a single power-law index $\alpha_{\lambda} = -1.32$ (Sec. 3.2). The observed F277W magnitude is 0.7 mag brighter than that expected from the continuum flux at F277W, which is significantly larger than the photometric error (0.2 mag). This excess is consistent with a luminosity for the $\text{H}\beta + [\text{O III}]$ lines of $L_{\text{H}\beta + [\text{O III}]} = 10^{43.0} \text{ erg s}^{-1}$ and rest-frame equivalent width $\text{EW}_{\text{H}\beta + [\text{O III}]} = 1100 \text{ Å}$. The $\text{H}\alpha$ excess in F410M and F444W, 1.2 and 0.6 mag, respectively, is explained by a strong $\text{H}\alpha$ emission with line luminosity

$L_{\text{H}\alpha} = 10^{42.9} \text{ erg s}^{-1}$ and rest-frame equivalent width $\text{EW}_{\text{H}\alpha} = 1600 \text{ Å}$. In addition, assuming the relation of $L_{\text{H}\alpha} = 3.1 L_{\text{H}\beta}$ expected for Case B’ recombination (e.g., Greene & Ho 2005), we infer the $[\text{O III}]$ luminosity as $L_{[\text{O III}]} \simeq 10^{42.9} \text{ erg s}^{-1}$. Note that these measurements slightly increase by 5 and 1 % for $\text{H}\beta + [\text{O III}]$ and $\text{H}\alpha$, respectively, when the second continuum model for $\alpha_{\lambda} = -1.27$ is used.

The two equivalent widths for $\text{H}\beta + [\text{O III}]$ and $\text{H}\alpha$ are extremely large as an AGN. The composite spectrum of low-redshift quasars of VB01 shows $\text{EW}_{\text{H}\beta + [\text{O III}]} \simeq 63 \text{ Å}$ and $\text{EW}_{\text{H}\alpha} \simeq 195 \text{ Å}$. The brightest type 2 quasars in the local universe show equivalently strong $[\text{O III}]$ line emission (both in terms of luminosity and equivalent width) (e.g., Zakamska et al. 2003; Kong & Ho 2018), while their bolometric luminosity estimated from the extinction-corrected $[\text{O III}]$ luminosity $L_{\text{bol}} \sim 10^{47} \text{ erg s}^{-1}$ is $\gtrsim 100$ times higher than that of CEERS-AGN-z5-1 (Heckman et al. 2004). We also note that the estimated $\text{H}\alpha$ luminosity of CEERS-AGN-z5-1 is five times higher than expected from the empirical relation between the $\text{H}\alpha$ luminosity and the 5100 Å luminosity for low-redshift broad-line AGNs (Greene & Ho 2005, their equation 1).

Alternatively, strong Balmer emission lines can also be produced from star-forming galaxies. Such high values of $\text{EW}_{\text{H}\alpha} \simeq 1000 \text{ Å}$ have been reported in $z > 6$ star-forming galaxies based on Spitzer and JWST (e.g., Endsley et al. 2021; Chen et al. 2022; Stefanon et al. 2022). However, those galaxies show a significantly steeper continuum slopes ($\alpha_{\lambda} \simeq -2.0$), compared to that of CEERS-AGN-z5-1. We will discuss the possible contribution of star-forming galaxies to the SED of CEERS-AGN-z5-1 in Section 4.1.

4. DISCUSSION

4.1. SED Fitting

The available photometry of CEERS-AGN-z5-1 continuously covers the SED from $\text{Ly}\alpha$ to $\text{H}\alpha$. We here present our SED fitting analysis with templates of metal-poor galaxies, low-redshift quasars, and super-Eddington accreting BHs. The redshift range is limited to $4.0 \leq z \leq 6.0$ (with steps of 0.01), which is wide enough to cover the redshifted $\text{H}\alpha$ emission with F410M.

4.1.1. Metal-Poor Galaxies

First, we attempt to reproduce the observed photometric SED with galaxy templates. We here adopt the galaxy SED models from Inoue (2011), where nebular emission lines are included for various metallicities of $Z = 0.02 (Z_{\odot})$, 0.008, 0.004, 0.0004, 10^{-5} , 10^{-7} , and 0.0 (no metals). The stellar mass spectrum is calculated by assuming a Salpeter initial mass function (IMF) with

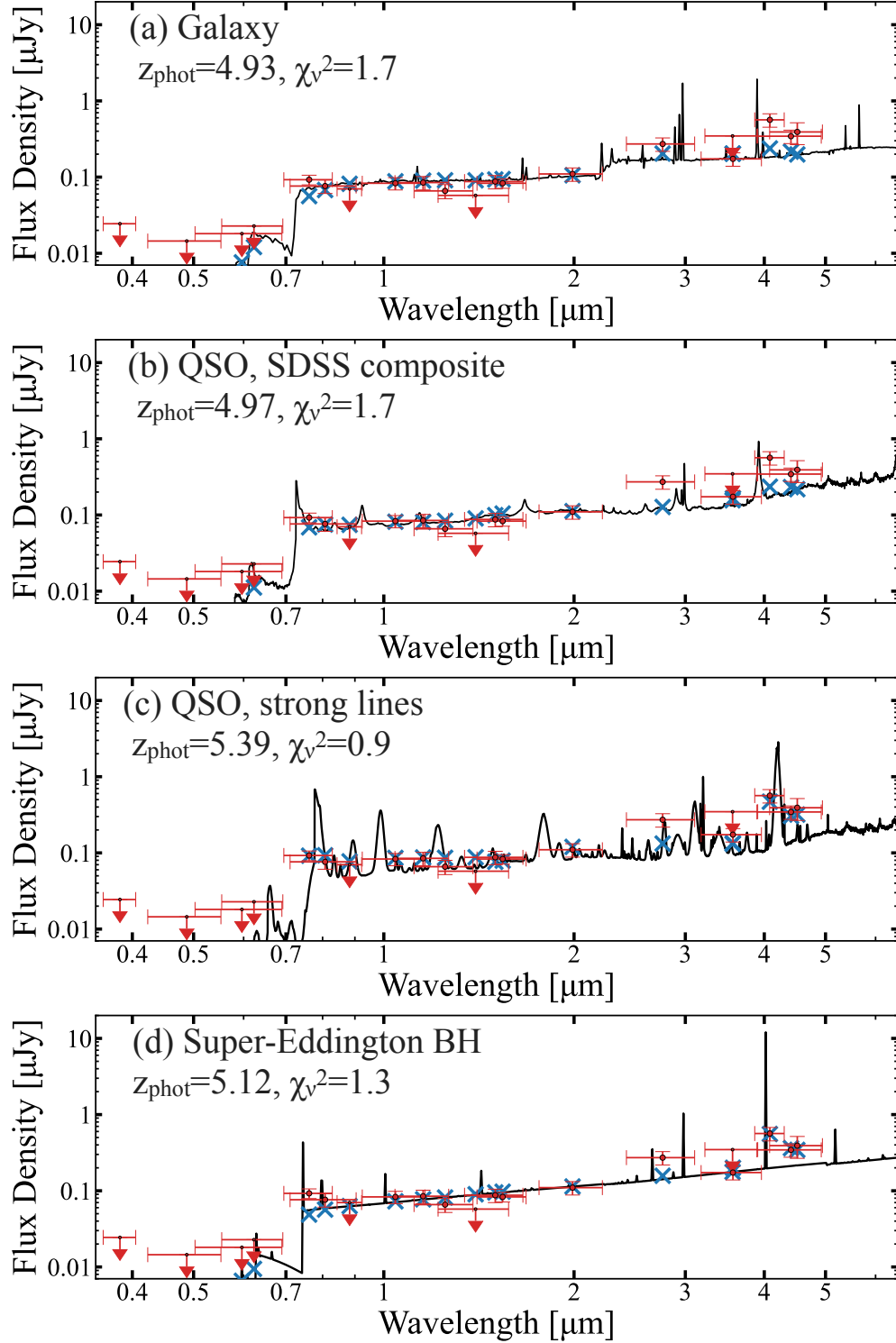


Figure 3. The results of our SED fitting. In each panel, we show the best-fit model of galaxies or AGNs with a black line. The photometric redshift and the reduced-chisquare of the best-fit model is shown at the upper left of each panel. The observed photometry is shown in red dot and the filter-convolved magnitudes of the best-fit models in blue cross. (a) The best-fit galaxy model from Inoue (2011)’s metal-poor galaxies. This model has a SMC-like dust extinction with color excess $E(B - V) = 0.05$. (b) The low-redshift composite quasar spectrum of Vanden Berk et al. (2001) scaled to match the photometry of CEERS-AGN-z5-1. (c) The same low-redshift composite spectrum with emission lines added to match $H\alpha$. See the text for the details of the procedure. (d) The SED model of an accreting super-Eddington BH (Inayoshi et al. 2022a). The scale of the best-fit model corresponds to the central BH mass of $M_{\text{BH}} = 10^{6.3} M_{\odot}$.

$1 - 100 M_{\odot}$ and a constant star formation rate (SFR) with a duration of 100 or 500 Myr. We also take into account dust attenuation by an extinction law of Small Magellanic Cloud (SMC; [Prevot et al. 1984](#); $R_v = 2.7$) to reproduce the red colors of CEERS-AGN-z5-1. Inter-galactic medium absorption is taken into account with the prescription of [Madau \(1995\)](#).

Figure 3(a) shows our best-fit model at $z = 4.93$ (reduced chisquare $\chi^2_{\nu} = 1.7$) with a metallicity of $Z = 0.004$, stellar age of 500 Myr, $\text{SFR} = 2.5 M_{\odot} \text{ yr}^{-1}$, and $E(B - V) = 0.05$. This model can partially explain the observed continuum at shorter wavelengths owing to dust attenuation, and the filter-convolved F277W flux density is raised by strong [O III] emission due to active starbursts. However, the model SED begins to mismatch at $> 4 \mu\text{m}$ and hardly reproduces the observed flux density at F410M, F444W, and IRAC $4.5 \mu\text{m}$. We also applied models with a shorter 10 Myr star-formation duration that have stronger [O III] emission. Those young galaxy models can also reproduce the continuum at $\lesssim 2 \mu\text{m}$ and the F277W excess as well as the former model, but the goodness-of-fit gets worse by $\Delta\chi^2_{\nu} = +0.7$ due to insufficient continuum emission at longer wavelengths. Therefore, these pure galaxy models are not favored to explain CEERS-AGN-z5-1.

4.1.2. AGNs with Strong Emission Lines

Next, we test the composite spectrum of low-redshift quasars compiled by [VB01](#). This composite spectrum from the SDSS covers the rest-wavelength 800–8555 Å and includes 80 resolved emission-line features in the spectrum. The continuum index measured at rest-frame 1300–5000 Å is $\alpha_{\lambda} = -1.56$. Figure 3(b) shows the scaled spectrum at $z = 4.97$ matched to CEERS-AGN-z5-1 ($\chi^2_{\nu} = 1.7$). This model agrees with the observed continuum of CEERS-AGN-z5-1 well; however, the broad/medium-band excess due to $\text{H}\beta + [\text{O III}]$ and $\text{H}\alpha$ is not sufficiently reproduced (Section 3.3).

The composite spectrum of [VB01](#) is constructed based on luminous quasars, unlike CEERS-AGN-z5-1. It is observationally known that the strength of quasar emission lines increases as the continuum luminosity decreases ([Baldwin 1977](#)). To mimic the so-called Baldwin effect, we increase the strength of *all* the emission lines listed in Table 2 of [VB01](#), so that the relative flux ratio of each line is maintained⁶. We add those additional emission line fluxes to the original spectrum assuming Gaussian profiles with the same line widths as those measured in [VB01](#). This modified version of the [VB01](#)’s quasar SED

model is presented in Figure 3(c), in which case a better goodness-of-fit is achieved at $z = 5.39$ ($\chi^2_{\nu} = 0.9$) than the original composite spectrum. The excess of $\text{Ly}\alpha$ and $\text{H}\alpha$ is better reproduced than the original model in this case, however the observed flux density at F277W is still twice higher than predicted from this third model.

4.1.3. Super-Eddington Accreting BHs

As an alternative scenario, we consider more theory-based SED model for a super-Eddington accreting BH with $M_{\text{BH}} \sim 10^6 M_{\odot}$ ([Inayoshi et al. 2022b](#)). The SED-model is constructed by post-process line transfer calculations with CLOUDY (C17; [Ferland et al. 2017](#)), which is applied to the results of radiation hydrodynamical simulations of a seed BH rapidly growing in the proto-galactic nucleus ([Inayoshi et al. 2022a](#)). In this model, several prominent lines are powered by the central BH fed via a dense accretion disk at super-Eddington rates. Among them, strong $\text{H}\alpha$ line emission with a rest-frame $\text{EW}_{\text{H}\alpha} \simeq 1300 \text{ Å}$ is so prominent that the line flux affects the broad-band colors significantly, just like we observe in CEERS-AGN-z5-1.

Figure 3(d) shows the best-fit model of a super-Eddington accreting BH ($\chi^2_{\nu} = 1.3$) scaled to $z = 5.12$. This model explains the continuum flux densities and the broad/medium-band excess in F410M, F444W, and IRAC $4.5 \mu\text{m}$, owing to the strong $\text{H}\alpha$ emission powered by the fast-growing BH. The overall flux normalization of the best-fit case is only 1.4 times higher compared to the original SED model, suggesting that the predicted line information (e.g., low-ionization emission lines of C II] $\lambda 2326$ and O I] $\lambda \lambda 1304$) is still valid and can be tested by follow-up spectroscopic observations of CEERS-AGN-z5-1. This model yields a slightly larger χ^2_{ν} value compared to the quasar model with enhanced emission lines (Fig. 3(c)), but we note that the SED model for a super-Eddington BH does not include the broad-line components that could be produced in the inner region but are unresolved in their simulations.

4.2. Possible Contribution of [O III] from Host Galaxy

Based on our SED fitting analysis, two scenarios are favored to explain the observed SED for CEERS-AGN-z5-1: an unobscured AGN with strong broad-line emission (Fig. 3c) and a super-Eddington accreting BH (Fig. 3d). However, neither of the two cases can fully explain the broad-band excess of F277W. We hypothesize that this excess is at least partly attributed to the actively star-forming host galaxy radiating strong [O III] emission line.

One may consider an extremely young galaxy with age $\lesssim 10 \text{ Myr}$, as is discussed in the literature (e.g., [Inoue 2011](#); [Wilkins et al. 2020](#); [Tang et al. 2021](#)). With the

⁶ We do not increase the strength of the unresolved iron pseudo-continuum in the original spectrum.

Inoue (2011)’s galaxy model with $Z = 0.004$ and age = 10 Myr, the [O III] luminosity can be as strong as what is required to explain the observed magnitude in F277W, when the host SFR is $\sim 10 M_{\odot} \text{ yr}^{-1}$. This galaxy model, however, predicts a stellar mass of $M_{\star} \lesssim 10^8 M_{\odot}$, which is substantially lower than that expected from the canonical BH-to-galaxy mass ratio of $M_{\star} \sim 200 M_{\text{BH}}$ observed in the local universe (Kormendy & Ho 2013)⁷. We note that this order estimate does not consider the contribution of the host to other filters.

Alternatively, a top-heavy stellar IMF expected in metal-poor environments can also be another solution to produce strong [O III] emission lines from galaxies, which is not taken into account in the galaxy models we use in this paper. It is also possible that the nebular gas is oxygen-rich in low metallicity relative to the solar value, which enhances the strength of [O III] emission without changing the value of metallicity. The detailed modeling of galaxy SEDs is left for future investigation.

4.3. $z = 5$ AGN Luminosity Function

The discovery of the promising candidate of a high-redshift AGN was unexpected from the first CEERS dataset. To quantify the serendipity, we discuss the number density of $z \sim 5$ AGNs based on CEERS-AGN-z5-1. We caution that we can only provide a lower bound of the AGN luminosity function with this work especially because we do not consider AGNs embedded in their host galaxies with extended morphology. Such a population would be common for faint AGNs at UV magnitudes dominated by star-forming galaxies.

Figure 4 shows our estimate of the $z \sim 5$ AGN luminosity function. We calculate the binned number density as $\Phi = 1.03 \times 10^{-5} \text{ Mpc}^{-3} \text{ mag}^{-1}$ at $M_{1450} = -19.5$ mag (red), where we adopt the survey area of 34.5 arcmin² and set $z = 5.15$ and its interval of $\Delta z = \pm 0.5$ to calculate the cosmic volume. For comparison, we overlay the binned quasar luminosity functions derived from Subaru/HSC+SDSS (Niida et al. 2020), and CFHT Legacy Survey (McGreer et al. 2018). We also show the $z = 4.5$ X-ray detected AGN luminosity function in the CANDELS fields (including EGS), which go down to $M_{1450} = -18.5$ mag (Giallongo et al. 2019)⁸. In Figure 4, we take the face values of their $z = 4.5$ luminosity function without correcting for redshift evolution. The abundance of the faintest AGNs at $M_{1450} = -19.5$

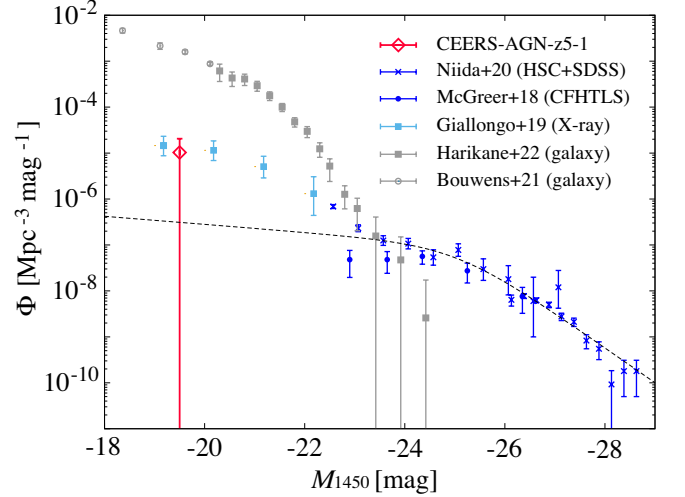


Figure 4. The $z \sim 5$ UV luminosity function of AGN. Our constraint from CEERS-AGN-z5-1 is shown in red. The quasar luminosity function data obtained from different surveys are shown: the rest-UV selected quasars combining Subaru HSC and SDSS (Niida et al. 2020, cross) and CFHTLS (McGreer et al. 2018, dot) in blue. The abundance of AGN at $M_{1450} = -19.5$ mag is significantly higher than the extrapolation of the rest-UV selected QLF (dashed line), while within the Poisson error from one object. Our data point is consistent with the AGN luminosity function from the X-ray detected AGN candidates in the CANDELS field (Giallongo et al. 2019), which are shown in cyan. Shown in grey are the UV luminosity function of galaxies from Bouwens et al. (2021, circle) and Harikane et al. (2022a, square).

mag is substantially higher than that expected from extrapolation of the HSC+SDSS QLFs (short dashed; Niida et al. 2020), while the extrapolation of their double power-law LF is still consistent with our data point within the Poisson error of one object. Intriguingly, our binned luminosity function is rather consistent with those of Chandra-detected (0.5–2 keV) X-ray sources from Giallongo et al. (2019), while we caution that neither of them are spectroscopically confirmed.

5. FUTURE PROSPECTS

Spectroscopic follow-up observations are the key to confirming the redshift and the nature of CEERS-AGN-z5-1, and also our estimate of the $z = 5$ AGN luminosity function at the very faint end, where galaxies are dominant against AGNs in number (Figure 4). Fortunately, the CEERS6 field, where the source resides in, is going to be followed up with JWST’s NIRSpec Micro-Shutter Assembly and NIRCам Wide Field Slitless Spectroscopy in December 2022. Those observations will also help to test the extreme emission-line properties that we discuss in Sections 3.3 and 4.1. Specifically, detection of broad-line emission will enable us to perform a virial

⁷ In contrast, the existence of an overmassive BH relative to its host galaxy ($M_{\star} \sim 10^2 M_{\text{BH}}$) is consistent with the necessary conditions for the onset of super-Eddington accretion onto a BH embedded in a compact bulge (Inayoshi et al. 2022a).

⁸ CEERS-AGN-z5-1 is not a part of their AGN candidates.

BH mass estimate via Balmer lines or other mass tracers such as Mg II, from which one can constrain the mass distribution of seed BHs in the earlier epochs of the universe (Toyouchi et al. 2022; see also Inayoshi et al. 2020; Greene et al. 2020).

Our initial result based on the first observations of the CEERS program indicates that deep NIR imaging observations of JWST are capable of determining the high-redshift AGN luminosity function at the very faint end. More complete and sophisticated AGN selection criteria are required to better constrain the underlying AGN population. Ongoing and upcoming wide-field surveys with JWST such as COSMOS Web and JADES programs can also be used to perform wider and deeper surveys of high-redshift AGNs.

We wish to thank the entire JWST team and the CEERS collaboration for the operation of the telescope and for developing their observing program with a zero-exclusive-access period. This work is based on observations made with the NASA/ESA/CSA James Webb Space Telescope. The data were obtained from the Mikulski Archive for Space Telescopes at the Space Telescope Science Institute, which is operated by the Association of Universities for Research in Astronomy, Inc., under NASA contract NAS 5-03127 for JWST. These observations are associated with program 1345.

This work has made use of data from the European Space Agency (ESA) mission *Gaia* (<https://www.cosmos.esa.int/gaia>), processed by the *Gaia* Data Processing and Analysis Consortium (DPAC, <https://www.cosmos.esa.int/web/gaia/dpac/consortium>). Funding for the DPAC has been provided by national institutions, in particular the institutions participating in the *Gaia* Multilateral Agreement.

We acknowledge support from the National Natural Science Foundation of China (12150410307, 12073003, 12003003, 11721303, 11991052, 11950410493), and the China Manned Space Project Nos. CMS-CSST-2021-A04 and CMS-CSST-2021-A06. X. D. is supported by JSPS KAKENHI Grant Number JP22K14071.

Facilities: JWST, HST, Spitzer, CFHT, GAIA

Software: astropy (Astropy Collaboration et al. 2013), Galight (Ding et al. 2020, 2021), Photutils (Bradley et al. 2022), SExtractor (Bertin & Arnouts 1996), STScI JWST Calibration Pipeline (jwst-pipeline.readthedocs.io)

REFERENCES

- Adams, N. J., Bowler, R. A. A., Jarvis, M. J., Varadaraj, R. G., & Häußler, B. 2022a, arXiv e-prints, arXiv:2207.09342. <https://arxiv.org/abs/2207.09342>
- Adams, N. J., Conselice, C. J., Ferreira, L., et al. 2022b, arXiv e-prints, arXiv:2207.11217. <https://arxiv.org/abs/2207.11217>
- Astropy Collaboration, Robitaille, T. P., Tollerud, E. J., et al. 2013, A&A, 558, A33, doi: [10.1051/0004-6361/201322068](https://doi.org/10.1051/0004-6361/201322068)
- Bañados, E., Venemans, B. P., Mazzucchelli, C., et al. 2018, Nature, 553, 473, doi: [10.1038/nature25180](https://doi.org/10.1038/nature25180)
- Baldwin, J. A. 1977, ApJ, 214, 679, doi: [10.1086/155294](https://doi.org/10.1086/155294)
- Bertin, E., & Arnouts, S. 1996, A&AS, 117, 393, doi: [10.1051/aas:1996164](https://doi.org/10.1051/aas:1996164)
- Bouwens, R. J., Oesch, P. A., Stefanon, M., et al. 2021, AJ, 162, 47, doi: [10.3847/1538-3881/abf83e](https://doi.org/10.3847/1538-3881/abf83e)
- Bowler, R. A. A., Adams, N. J., Jarvis, M. J., & Häußler, B. 2021, MNRAS, 502, 662, doi: [10.1093/mnras/stab038](https://doi.org/10.1093/mnras/stab038)
- Bradley, L., Sipőcz, B., Robitaille, T., et al. 2022, astropy/photutils, 1.4.0, Zenodo, Zenodo, doi: [10.5281/zenodo.6385735](https://doi.org/10.5281/zenodo.6385735)
- Castellano, M., Fontana, A., Treu, T., et al. 2022, arXiv e-prints, arXiv:2207.09436. <https://arxiv.org/abs/2207.09436>
- Chen, Z., Stark, D. P., Endsley, R., et al. 2022, arXiv e-prints, arXiv:2207.12657. <https://arxiv.org/abs/2207.12657>

- Ding, X., Birrer, S., Treu, T., & Silverman, J. D. 2021, arXiv e-prints, arXiv:2111.08721. <https://arxiv.org/abs/2111.08721>
- Ding, X., Silverman, J. D., & Onoue, M. 2022, arXiv e-prints, arXiv:2209.03359. <https://arxiv.org/abs/2209.03359>
- Ding, X., Silverman, J., Treu, T., et al. 2020, ApJ, 888, 37, doi: [10.3847/1538-4357/ab5b90](https://doi.org/10.3847/1538-4357/ab5b90)
- Donnan, C. T., McLeod, D. J., Dunlop, J. S., et al. 2022, arXiv e-prints, arXiv:2207.12356. <https://arxiv.org/abs/2207.12356>
- Endsley, R., Stark, D. P., Chevallard, J., & Charlot, S. 2021, MNRAS, 500, 5229, doi: [10.1093/mnras/staa3370](https://doi.org/10.1093/mnras/staa3370)
- Fan, X., Narayanan, V. K., Lupton, R. H., et al. 2001a, AJ, 122, 2833, doi: [10.1086/324111](https://doi.org/10.1086/324111)
- Fan, X., Strauss, M. A., Richards, G. T., et al. 2001b, AJ, 121, 31, doi: [10.1086/318032](https://doi.org/10.1086/318032)
- Ferland, G. J., Chatzikos, M., Guzmán, F., et al. 2017, RMxAA, 53, 385. <https://arxiv.org/abs/1705.10877>
- Finkelstein, S. L., Dickinson, M., Ferguson, H. C., et al. 2017, The Cosmic Evolution Early Release Science (CEERS) Survey, JWST Proposal ID 1345. Cycle 0 Early Release Science
- Finkelstein, S. L., Bagley, M. B., Arrabal Haro, P., et al. 2022, arXiv e-prints, arXiv:2207.12474. <https://arxiv.org/abs/2207.12474>
- Gaia Collaboration, Prusti, T., de Bruijne, J. H. J., et al. 2016, A&A, 595, A1, doi: [10.1051/0004-6361/201629272](https://doi.org/10.1051/0004-6361/201629272)
- Giallongo, E., Grazian, A., Fiore, F., et al. 2019, ApJ, 884, 19, doi: [10.3847/1538-4357/ab39e1](https://doi.org/10.3847/1538-4357/ab39e1)
- Goulding, A. D., & Greene, J. E. 2022, arXiv e-prints, arXiv:2208.02822. <https://arxiv.org/abs/2208.02822>
- Greene, J. E., & Ho, L. C. 2005, ApJ, 630, 122, doi: [10.1086/431897](https://doi.org/10.1086/431897)
- . 2007, ApJ, 670, 92, doi: [10.1086/522082](https://doi.org/10.1086/522082)
- Greene, J. E., Strader, J., & Ho, L. C. 2020, ARA&A, 58, 257, doi: [10.1146/annurev-astro-032620-021835](https://doi.org/10.1146/annurev-astro-032620-021835)
- Harikane, Y., Ono, Y., Ouchi, M., et al. 2022a, ApJS, 259, 20, doi: [10.3847/1538-4365/ac3dfc](https://doi.org/10.3847/1538-4365/ac3dfc)
- Harikane, Y., Ouchi, M., Oguri, M., et al. 2022b, arXiv e-prints, arXiv:2208.01612. <https://arxiv.org/abs/2208.01612>
- Heckman, T. M., Kauffmann, G., Brinchmann, J., et al. 2004, ApJ, 613, 109, doi: [10.1086/422872](https://doi.org/10.1086/422872)
- Hu, H., Inayoshi, K., Haiman, Z., et al. 2022, ApJ, 935, 140, doi: [10.3847/1538-4357/ac7daa](https://doi.org/10.3847/1538-4357/ac7daa)
- Inayoshi, K., Nakatani, R., Toyouchi, D., et al. 2022a, ApJ, 927, 237, doi: [10.3847/1538-4357/ac4751](https://doi.org/10.3847/1538-4357/ac4751)
- Inayoshi, K., Onoue, M., Sugahara, Y., Inoue, A. K., & Ho, L. C. 2022b, ApJL, 931, L25, doi: [10.3847/2041-8213/ac6f01](https://doi.org/10.3847/2041-8213/ac6f01)
- Inayoshi, K., Visbal, E., & Haiman, Z. 2020, ARA&A, 58, 27, doi: [10.1146/annurev-astro-120419-014455](https://doi.org/10.1146/annurev-astro-120419-014455)
- Inoue, A. K. 2011, MNRAS, 415, 2920, doi: [10.1111/j.1365-2966.2011.18906.x](https://doi.org/10.1111/j.1365-2966.2011.18906.x)
- Jiang, L., McGreer, I. D., Fan, X., et al. 2016, ApJ, 833, 222, doi: [10.3847/1538-4357/833/2/222](https://doi.org/10.3847/1538-4357/833/2/222)
- Jiang, L., Ning, Y., Fan, X., et al. 2022, Nature Astronomy, 6, 850, doi: [10.1038/s41550-022-01708-w](https://doi.org/10.1038/s41550-022-01708-w)
- Kato, N., Matsuoka, Y., Onoue, M., et al. 2020, PASJ, 72, 84, doi: [10.1093/pasj/psaa074](https://doi.org/10.1093/pasj/psaa074)
- Kong, M., & Ho, L. C. 2018, ApJ, 859, 116, doi: [10.3847/1538-4357/aabe2a](https://doi.org/10.3847/1538-4357/aabe2a)
- Kormendy, J., & Ho, L. C. 2013, ARA&A, 51, 511, doi: [10.1146/annurev-astro-082708-101811](https://doi.org/10.1146/annurev-astro-082708-101811)
- Laporte, N., Nakajima, K., Ellis, R. S., et al. 2017, ApJ, 851, 40, doi: [10.3847/1538-4357/aa96a8](https://doi.org/10.3847/1538-4357/aa96a8)
- Liu, H.-Y., Liu, W.-J., Dong, X.-B., et al. 2019, ApJS, 243, 21, doi: [10.3847/1538-4365/ab298b](https://doi.org/10.3847/1538-4365/ab298b)
- Liu, H.-Y., Yuan, W., Dong, X.-B., Zhou, H., & Liu, W.-J. 2018, ApJS, 235, 40, doi: [10.3847/1538-4365/aab88e](https://doi.org/10.3847/1538-4365/aab88e)
- Madau, P. 1995, ApJ, 441, 18, doi: [10.1086/175332](https://doi.org/10.1086/175332)
- Matsuoka, Y., Strauss, M. A., Kashikawa, N., et al. 2018, ApJ, 869, 150, doi: [10.3847/1538-4357/aaee7a](https://doi.org/10.3847/1538-4357/aaee7a)
- Matsuoka, Y., Onoue, M., Kashikawa, N., et al. 2019, ApJL, 872, L2, doi: [10.3847/2041-8213/ab0216](https://doi.org/10.3847/2041-8213/ab0216)
- McGreer, I. D., Fan, X., Jiang, L., & Cai, Z. 2018, AJ, 155, 131, doi: [10.3847/1538-3881/aaaab4](https://doi.org/10.3847/1538-3881/aaaab4)
- Morishita, T., Stiavelli, M., Trenti, M., et al. 2020, ApJ, 904, 50, doi: [10.3847/1538-4357/abba83](https://doi.org/10.3847/1538-4357/abba83)
- Naidu, R. P., Oesch, P. A., Setton, D. J., et al. 2022, arXiv e-prints, arXiv:2208.02794. <https://arxiv.org/abs/2208.02794>
- Natarajan, P., Pacucci, F., Ferrara, A., et al. 2017, ApJ, 838, 117, doi: [10.3847/1538-4357/aa6330](https://doi.org/10.3847/1538-4357/aa6330)
- Neeleman, M., Novak, M., Venemans, B. P., et al. 2021, ApJ, 911, 141, doi: [10.3847/1538-4357/abe70f](https://doi.org/10.3847/1538-4357/abe70f)
- Netzer, H. 2019, MNRAS, 488, 5185, doi: [10.1093/mnras/stz2016](https://doi.org/10.1093/mnras/stz2016)
- Niida, M., Nagao, T., Ikeda, H., et al. 2020, ApJ, 904, 89, doi: [10.3847/1538-4357/abbe11](https://doi.org/10.3847/1538-4357/abbe11)
- Onoue, M., Kashikawa, N., Matsuoka, Y., et al. 2019, ApJ, 880, 77, doi: [10.3847/1538-4357/ab29e9](https://doi.org/10.3847/1538-4357/ab29e9)
- Prevot, M. L., Lequeux, J., Maurice, E., Prevot, L., & Rocca-Volmerange, B. 1984, A&A, 132, 389
- Richards, G. T., Lacy, M., Storrie-Lombardi, L. J., et al. 2006, The Astrophysical Journal Supplement Series, 166, 470, doi: [10.1086/506525](https://doi.org/10.1086/506525)

- Rieke, M. J., Kelly, D., & Horner, S. 2005, in Society of Photo-Optical Instrumentation Engineers (SPIE) Conference Series, Vol. 5904, Cryogenic Optical Systems and Instruments XI, ed. J. B. Heaney & L. G. Burriesci, 1–8, doi: [10.1117/12.615554](https://doi.org/10.1117/12.615554)
- Shen, Y., Richards, G. T., Strauss, M. A., et al. 2011, The Astrophysical Journal Supplement Series, 194, 45, doi: [10.1088/0067-0049/194/2/45](https://doi.org/10.1088/0067-0049/194/2/45)
- Shen, Y., Wu, J., Jiang, L., et al. 2019, ApJ, 873, 35, doi: [10.3847/1538-4357/ab03d9](https://doi.org/10.3847/1538-4357/ab03d9)
- Shi, Y., Kremer, K., Grudić, M. Y., Gerling-Dunsmore, H. J., & Hopkins, P. F. 2022, arXiv e-prints, arXiv:2208.05025. <https://arxiv.org/abs/2208.05025>
- Stefanon, M., Bouwens, R. J., Illingworth, G. D., et al. 2022, ApJ, 935, 94, doi: [10.3847/1538-4357/ac7e44](https://doi.org/10.3847/1538-4357/ac7e44)
- Stefanon, M., Yan, H., Mobasher, B., et al. 2017, ApJS, 229, 32, doi: [10.3847/1538-4365/aa66cb](https://doi.org/10.3847/1538-4365/aa66cb)
- Tang, M., Stark, D. P., Chevallard, J., et al. 2021, MNRAS, 503, 4105, doi: [10.1093/mnras/stab705](https://doi.org/10.1093/mnras/stab705)
- Toyouchi, D., Inayoshi, K., Li, W., Haiman, Z., & Kuiper, R. 2022, arXiv e-prints, arXiv:2206.14459. <https://arxiv.org/abs/2206.14459>
- Trakhtenbrot, B., Netzer, H., Lira, P., & Shemmer, O. 2011, ApJ, 730, 7, doi: [10.1088/0004-637X/730/1/7](https://doi.org/10.1088/0004-637X/730/1/7)
- Valiante, R., Schneider, R., Zappacosta, L., et al. 2018, MNRAS, 476, 407, doi: [10.1093/mnras/sty213](https://doi.org/10.1093/mnras/sty213)
- Vanden Berk, D. E., Richards, G. T., Bauer, A., et al. 2001, AJ, 122, 549, doi: [10.1086/321167](https://doi.org/10.1086/321167)
- Walter, F., Neeleman, M., Decarli, R., et al. 2022, ApJ, 927, 21, doi: [10.3847/1538-4357/ac49e8](https://doi.org/10.3847/1538-4357/ac49e8)
- Wang, F., Yang, J., Fan, X., et al. 2021, ApJL, 907, L1, doi: [10.3847/2041-8213/abd8c6](https://doi.org/10.3847/2041-8213/abd8c6)
- Wilkins, S. M., Lovell, C. C., Fairhurst, C., et al. 2020, MNRAS, 493, 6079, doi: [10.1093/mnras/staa649](https://doi.org/10.1093/mnras/staa649)
- Willott, C. J., Albert, L., Arzoumanian, D., et al. 2010, AJ, 140, 546, doi: [10.1088/0004-6256/140/2/546](https://doi.org/10.1088/0004-6256/140/2/546)
- Wu, X.-B., Wang, F., Fan, X., et al. 2015, Nature, 518, 512, doi: [10.1038/nature14241](https://doi.org/10.1038/nature14241)
- Yang, J., Wang, F., Fan, X., et al. 2021, ApJ, 923, 262, doi: [10.3847/1538-4357/ac2b32](https://doi.org/10.3847/1538-4357/ac2b32)
- Yuan, F., & Narayan, R. 2014, ARA&A, 52, 529, doi: [10.1146/annurev-astro-082812-141003](https://doi.org/10.1146/annurev-astro-082812-141003)
- Zakamska, N. L., Strauss, M. A., Krolik, J. H., et al. 2003, AJ, 126, 2125, doi: [10.1086/378610](https://doi.org/10.1086/378610)